Journal of Structural Geology 87 (2016) 134–143

Contents lists available at ScienceDirect

Journal of Structural Geology

journal homepage: www.elsevier.com/locate/jsg

Structural consequences of cohesion in gravitational instabilities triggered by fluid overpressure: Analytical derivation and experimental testing

R. Mourgues [a, *], A.C.G. Costa [b, c], F.O. Marques [d], A. Lacoste [e], A. Hildenbrand [c]

[a] L.P.G., UMR-CNRS 6112, Université du Maine, 72089 Le Mans, France
[b] Universidade de Lisboa and IDL, Lisboa, Portugal
[c] GEOPS, Univ. Paris-Sud, CNRS, Université Paris-Saclay, Rue du Belvédère, Bât. 504-509, 91405 Orsay, France
[d] Universidade de Lisboa, Lisboa, Portugal
[e] GeHCO, E.A.6293, Université de Tours, Tours, France

ARTICLE INFO

Article history:
Received 12 October 2015
Received in revised form
28 March 2016
Accepted 6 April 2016
Available online 13 April 2016

Keywords:
Gravitational spreading
Landslide
Effect of cohesion
Fluid overpressure
Critical taper theory
Listric faults

ABSTRACT

The critical taper theory of Coulomb wedges has been classically applied to compressive regimes (accretionary prisms/fold-and-thrust belts), and more recently to gravitational instabilities. Following the initial hypothesis of the theory, we provide an alternative expression of the exact solution for a non-cohesive wedge by considering the balance of forces applied to the external surfaces. Then, we use this approach to derive a solution for the case of cohesive wedges. We show that cohesion has conspicuous structural effects, including a minimum length required for sliding and the formation of listric faults. The stabilizing effect of cohesion is accentuated in the foremost thin domain of the wedge, defining a required Minimum Failure Length (MFL), and producing sliding of a rigid mass above the detachment. This MFL decreases with less cohesion, a smaller coefficient of internal friction, larger fluid overpressure ratio, and steeper upper and basal surfaces for the wedge. Listricity of the normal faults depends on the fluid overpressure magnitude within the wedge. For moderate fluid overpressure, normal faults are curved close to the surface, and become straight at depth. In contrast, where fluid overpressure exceeds a critical value corresponding to the fluid pressure required to destabilize the surface of a noncohesive wedge, the state of stress changes and rotates at depth. The faults are straight close to the surface and listric at depth, becoming parallel to the upper surface if the wedge is thick enough. We tested some of these structural effects of a cohesive wedge on gravitational instabilities using analogue models where cohesive material was subjected to pore-fluid pressure. The shape of the faults obtained in the models is consistent with the predictions of the theory.

1. Introduction

Events of large-scale gravitational destabilization occur in a wide range of geological settings (e.g., Moore et al., 1989; Haflidason et al., 2004; Lacoste et al., 2009). Such events result from progressive changes in physical parameters that are critical for the stability state of a given slope (e.g., decrease of the material's strength and surface morphology due to weathering/erosion, sedimentation, tectonics, changes to pore-pressure conditions) (e.g., Voight and Elsworth, 1997; Masson et al., 2006). The identification of the factors leading to stability decrease matters greatly to geosciences hazard analysis with respect to society and the economy (e.g., geotechnics and civil engineering, volcanology, oil industry).

However, in many cases, only the surface deformation or the scar/deposits are detectable (e.g., Hildenbrand et al., 2012; Costa et al., 2014). Geophysical methods characterize the geometry of the basal detachment and nature of the internal deformation of the displaced volume (Morgan et al., 2003; Haflidason et al., 2004). Geomechanical tests also provide helpful information, but sampling is sometimes difficult or impossible. Detailed structural analysis can be used to estimate indirectly some of the mechanical characteristics of the rocks involved in the unstable mass. Alternatively, efficient mathematical models are required to describe the various structural outcomes from the destabilization.

Among the destabilizing factors, high pore-fluid pressure is often invoked for causing low-dip slopes in sub-aerial and

* Corresponding author.
E-mail address: Regis.Mourgues@univ-lemans.fr (R. Mourgues).

http://dx.doi.org/10.1016/j.jsg.2016.04.008
0191-8141/

submarine structures at various scales: e.g., large-scale flank collapses in volcanic islands (Iverson, 1995; Day, 1996), sub-aerial landslides in active margins associated with river incision (Waitawhiti landslides, New Zealand – Lacoste et al., 2009, 2011), and submarine landslides affecting passive margins (Amazon Fan – Cobbold et al., 2004; Mourgues et al., 2009; Gulf of Mexico - Flemings et al., 2008; Storegga slide/North Sea Fan – Kvalstad et al., 2005b). Fluid overpressure is generated through several mechanisms, such as compaction disequilibrium (Walder and Nur, 1984; Day, 1996), mechanical and thermal pressurization of the porous medium (e.g., thermal and mechanic effects of magmatic intrusion, and associated effect of magmatic degassing – Iverson, 1995; Day, 1996; Elsworth and Voight, 1996; Voight and Elsworth, 1997; Reid, 2004), seismic loading (Elsworth and Voight, 1996), changing sea level (Iverson, 1995; Quidelleur et al., 2008; Smith et al., 2013), groundwater flow of meteoric water (Reid, 2004), and chemical reactions as in hydrocarbon generation (e.g., Cobbold et al., 2004, 2013; Zanella et al., 2014a, 2014b).

The critical taper model developed by Dahlen and co-authors is one of the most commonly used mathematical models for interpreting deformation systems having pore-fluid pressure (Davis et al., 1983; Dahlen et al., 1984; Dahlen, 1984, 1990). It has been widely applied to studying the shape of accretionary wedges and thrust belts, and estimating the weakness of basal detachments, often as a function of fluid pressure. A wedge of a Coulomb material subjected to lateral compression will deform internally until a critical taper forms. With this state, the prism and the basal detachment are everywhere on the verge of shear failure. Then, deformation will proceed with the growth of the wedge, including the self-similar growth for non-cohesive materials, through accretion of new material at the toe that maintains the critical taper and sliding along the basal detachment (Davis et al., 1983; Dahlen, 1984; Dahlen et al., 1984). The mathematical formulation of the critical taper has multiple solutions, depending on the shear orientation on the basal detachment and the stress state within the wedge (i.e., contractional or extensional).

Mourgues et al. (2014) pointed out that few studies focused on the applicability of the solution to gravitational spreading and gliding along passive margins, where elevated pore-fluid pressure is common in sediments, and where numerous gravitational structures, such as landslides and debris flows occur. Mourgues et al. (2014) investigated the applicability of the solution to gravitational instabilities for non-cohesive material with high pore-fluid pressure, in the absence of any external compressive or extensional forces. Mourgues et al. (2014) also proposed a mathematical expression differing from Dahlen (1984) for structural systems with gravitational instabilities, and they verified the predictions of the analytical model for slope instabilities by using physical experiments where compressed air was applied at the base of dry sand wedges to trigger gravitational instabilities (Mourgues and Cobbold, 2006a, 2006b; Lacoste et al., 2012). In their analysis, Mourgues et al. (2014) neglected the cohesion of the wedge, which was consistent with the prior work of Davis et al. (1983) and Dahlen (1984). However, cohesion is a critical parameter for rock strength, allowing for steep slopes and vertical cliffs to be stable, and therefore ideally should not be neglected in stability analysis (e.g., del Potro et al., 2013). In submarine settings, some landslides generate large blocks of undisrupted material, reflecting the initial cohesion of the sediments. Two famous major landslides present such characteristics: (1) the Storegga slide affected a sediment volume of 2400–3200 km^3 in the continental platform of the North Sea, with lateral spreading of large scale blocks (*Toreva* blocks) along 1.1–1.4° dipping failure surfaces (Haflidason et al., 2004; Bryn et al., 2005; Kvalstad et al., 2005a, 2005b); and (2) the Nu'uanu debris avalanche affected a volume of 2500–3500 km^3 in the NE of O'ahu Island in Hawaii, and involved the transport of a 30-km long and 600-km^3 block (the Tuscaloosa block) along ca. 55 km (Moore et al., 1989; Moore and Clague, 2002; Satake et al., 2002). The association of these major collapse events to fluid overpressure (Iverson, 1995; Kvalstad et al., 2005a) highlights the interest of studying the occurrence of gravitational destabilization assisted by fluid overpressure in cohesive materials.

Cohesion was first introduced in the critical taper model by Dahlen et al. (1984). These authors predicted that cohesion has a strong effect in the thinnest part of the wedge, while the deformation in the thickest part is similar to that of non-cohesive material (Davis et al., 1983; Dahlen et al., 1984). This implies that the upper surface of a Coulomb wedge will be concave: flatter in the foremost thinner sector more resistant to deformation, and steeper in the thicker sector where the slope tends towards that expected for a non-cohesive wedge (Davis et al., 1983).

Following the initial hypothesis of the Coulomb critical taper theory, we reformulate the analytical approach presented in Mourgues et al. (2014) to study the occurrence of gravitational destabilization in a cohesive wedge. We show that cohesion has conspicuous structural effects, including a minimum length of sliding and the formation of listric faults. This last prediction is then verified in the present study by physical experiments involving pore-fluids in cohesive and permeable granular materials.

2. The non-cohesive critical taper – a force equilibrium approach

The critical taper theory is based on the assumption that the internal state of stress of an homogeneous wedge composed of material deforming according to the Mohr-Coulomb criterion is on the verge of failure everywhere (Davis et al., 1983). The shape of the wedge, growing self-similarly, depends on the strength of the material, and on the relative magnitude of the basal friction.

2.1. Solutions derived from the equilibrium of internal stresses

Dahlen (1984) provided an exact solution for non-cohesive wedges by expressing the total taper angle of the critical wedge (expressed as the sum of the critical surface slope, α, and that of the basal detachment, β, Eq. (1)) as a function of pore pressure ratios (considered as constant) along the basal detachment (λ_b) and within the wedge (λ), coefficients of sliding friction along the basal detachment (μ_b) and within the wedge (μ):

$$\alpha + \beta = \Psi_o + \Psi_b \tag{1}$$

where Ψo and Ψb are the angles between the maximum principal stress and the upper surface or the basal detachment, respectively (Fig. 1a). These two angles are written more explicitly:

$$\Psi_o = 0.5 \arcsin\left(\frac{\sin \alpha'}{\sin \phi}\right) - 0.5\alpha' \tag{2}$$

with

$$\alpha' = \arctan\left(\frac{1}{1-\lambda^*}\tan \alpha\right) \tag{3}$$

$$\Psi_b = 0.5 \arcsin\left(\frac{\sin \phi'_b}{\sin \phi}\right) - 0.5\phi'_b \tag{4}$$

With ϕ the angle of friction of the wedge and ϕ'_b the effective angle of friction on the detachment, and defined by Dahlen (1984) as:

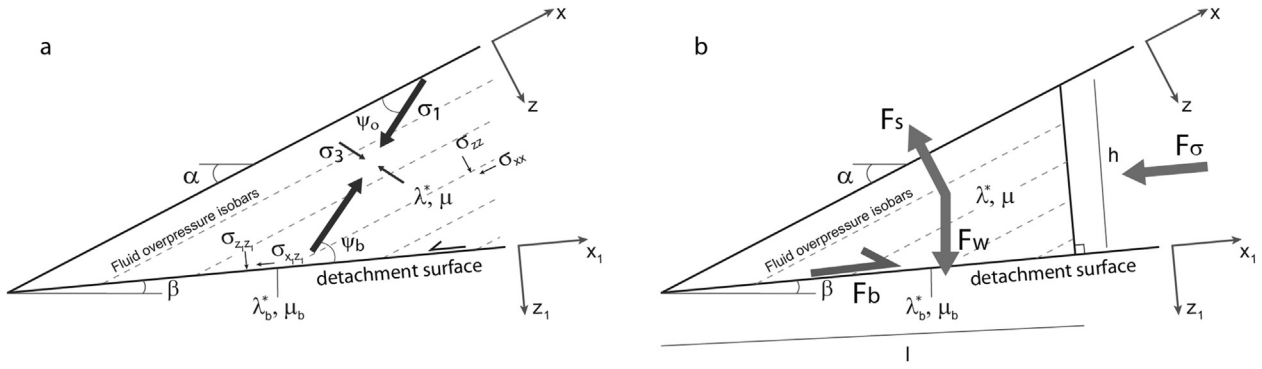

Fig. 1. a. Cross section of a wedge, showing the cartesian coordinates systems and variables used in the analysis (including Ψo and Ψb angles as used in Dahlen, 1984). **b**. Forces considered in the assessment of the wedge's stability along the basal detachment.

$$\mu'_b = \tan\phi'_b = \frac{1-\lambda^*_b}{1-\lambda^*}\mu_b \tag{5}$$

With λ^* the pore pressure ratio:

$$\lambda^* = \frac{P_{ov}}{\rho' g z \cos\alpha} \tag{6}$$

where ρ' is the density corrected for hydrostatic buoyancy ($\rho' = \rho - \rho_w$ with ρ the bulk density and ρ_w the density of water), g is the gravitational acceleration, and P_{ov} is the fluid overpressure (Hubbert and Rubey, 1959). P_{ov} is defined as the excess of pore pressure with reference to the hydrostatic pressure at the same depth (Mourgues and Cobbold, 2006b).

λ^* is defined within the wedge and λ^*_b is the pore-fluid overpressure ratio on the basal detachment.

Mourgues et al. (2014) provided an alternative formulation of Dahlen's expression (Dahlen, 1984) and Lehner's graphical solution (Lehner, 1986). Mourgues et al. (2014) expressed the fluid overpressure ratio (or the basal friction) required for the wedge to slide on a basal low-resistance layer as:

$$\lambda^*_b = 1 - \left(1-\lambda^*\right)\frac{E_2}{\mu_b E_1} \tag{7}$$

with

$$E_1 = \left(1-\lambda^*\right)\{Y + (1-Y)\cos[2(\alpha-\beta)]\} + \tan(\alpha)\sin[2(\alpha-\beta)] \tag{8}$$

$$E_2 = \left(1-\lambda^*\right)\{(Y-1)\sin[2(\alpha-\beta)]\} + \tan(\alpha)\cos[2(\alpha-\beta)] \tag{9}$$

$$Y = \frac{1-\sin\phi\sqrt{1-FS^2}}{\cos^2\phi} \quad \text{for a tensile state of stress} \tag{10}$$

$$Y = \frac{1+\sin\phi\sqrt{1-FS^2}}{\cos^2\phi} \quad \text{for a compressional state of stress} \tag{11}$$

and

$$FS = \frac{\tan\alpha}{\left(1-\lambda^*\right)\tan\phi} \tag{12}$$

This solution is better suited to the study of slope instabilities (Mourgues et al., 2014), and it provides important indications on the stability of the surface slope and the potential triggering of shallow slumps through the expression of the factor of safety FS (Eq. (12), and Fig. 2).

2.2. Solution derived from the balance of external forces applied on a triangular segment of the wedge

Equations (1) and (7) were derived from the equilibrium of internal stresses within the wedge. An alternative solution is to consider the balance of external forces applied on a triangular segment of the wedge. Dahlen used this approach in his review paper (Dahlen, 1990) to introduce the critical taper theory through a more intuitive approach, but he used a simplified state of stresses and did not derive the exact solution this way. In such an approach, the balance of forces applied on a triangular segment of length l and acting in the x_1 direction (Fig. 1b) is:

$$F_\sigma + F_w^{x1} + F_S^{x1} + F_b = 0 \tag{13}$$

F_σ is the force exerted by σ_{x1x1} on the sidewall of the wedge. F_w^{x1} is the x_1 component of the gravitational body force. F_s^{x1} is the net x_1 component of the force resulting from the pore-fluid pressure (seepage force), and F_b is the frictional force exerted at the base. Detailed expressions of these forces are given in Appendix A.

An exact solution can be found for a non-cohesive wedge, by

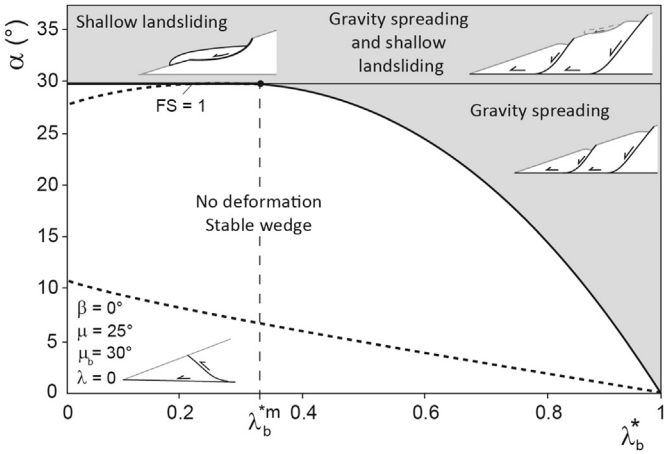

Fig. 2. Critical taper solutions for non-cohesive wedge given by equation (6). The dashed line represents the solution for a compressive state of stress. The black bold line represents the solution for a gravity-driven state of stress that yields extensional behavior. The grey area shows domains of slope instability triggered by gravity only. Gravitational spreading requires the detachment surface to be subjected to a minimal pore-fluid pressure (λ^{*m}_b). The line FS = 1 limits the area of shallow slides.

considering the static equilibrium of the system defined by Dahlen (1984) and expressions derived by Mourgues et al. (2014):

$$\lambda_b^* = 1 - \frac{1-\lambda^*}{E_1 \mu_b}\left[\left(E_3 + \lambda^*\right)\tan(\alpha-\beta) + \frac{\sin\beta}{\cos\alpha\cos(\alpha-\beta)}\right] \quad (14)$$

with

$$E_3 = \left(1-\lambda^*\right)(Y + (Y-1)\cos 2(\alpha-\beta)) - \tan\alpha \sin 2(\alpha-\beta) \quad (15)$$

Solutions 1, 7 and 13 are numerically identical. Wang et al. (2006), Mourgues et al. (2014) and Yuan et al. (2015) pointed out that the use of an effective angle of friction ϕ'_b (Eq. (5)) introduced by Dahlen is wrong, due to an error in the reference coordinate used to define λ. Mourgues et al. (2014) proposed a corrected value of the effective basal friction:

$$\mu'_b = \mu_b\left(1 + \frac{\lambda^* - \lambda_b^*}{E_1}\right) \quad (16)$$

and obtained an alternative solution for the critical taper. Using this corrected friction, Eq. (14) becomes:

$$\lambda_b^* = E_1 + \lambda^* - \frac{1}{\mu_b}\left[\left(E_3 + \lambda^*\right)\tan(\alpha-\beta) + \frac{\sin\beta}{\cos\alpha\cos(\alpha-\beta)}\right] \quad (17)$$

3. Gravitational instabilities in a cohesive wedge, and structural consequences

In the model derived from external forces (Section 2.2), cohesion was neglected. By introducing a significant cohesion within the wedge, F_σ is modified (see Appendix A). It also slightly changes F_b by modifying σ_{zz}. Cohesion induces non-linearity and a simple exact solution can no longer be found. Consequently, F_σ has to be numerically integrated and the solution of the force balance is iteratively found.

3.1. Minimal Failure Length (MFL)

On one hand, in a non-cohesive wedge, sliding along a low-resistance detachment plane can be triggered as soon as the gravitational potential of the system is large enough to overcome the basal frictional resistance. This behavior only requires the detachment surface to be subjected to a minimal pore-fluid pressure λ_b^{*m} (Fig. 2). This pressure value (Eq. (17)) does not depend on the length of the wedge, therefore driving and resisting forces are identical everywhere within the wedge (Figs. 3a and 4a), and normal faults may appear everywhere (Fig. 3a).

On the other hand, cohesion allows steeper stable slopes, by increasing the shear strength of the material. F_σ acts as a resisting force near the surface, and becomes a driving force at depth (Fig. 4b). Despite the wedge being considered everywhere on the verge of failure, the equilibrium of forces requires a Minimal Failure Length (*MFL*), as illustrated in Fig. 4b and c. The plot of the driving and resisting forces along the basal detachment (Fig. 3b) shows that for wedge lengths (L) smaller than the *MFL*, the driving force F_d is smaller than the resisting force F_b and the wedge remains stable along its basal detachment. In other words, no gravitational instabilities rooting on the basal detachment can develop in wedges having lengths shorter than the *MFL*. For wedges longer than the *MFL*, the first normal faults to form root on the basal detachment at a minimal distance from the toe (at least at the *MFL* distance). The *MFL* varies as a function of several factors. It increases with increasing cohesion and friction values in the wedge and along the basal detachment, and it decreases with increasing pore pressure (λ^* and λ^*_b). Therefore, if the pore pressure progressively increases, then the *MFL* becomes smaller than the length of the wedge L. Formation of the normal faults will occur, at least at an *MFL* distance from the front of the wedge, while the frontal/thinner segment of the wedge ($L < MFL$) will slide along the basal detachment without internal deformation (Fig. 3b). This is an important difference with non-cohesive wedges, where deformation may start everywhere in the wedge (Figs. 3a and 4a). The necessary *MFL* and the formation of a sliding mass with no major internal deformation are some aspects that are also observed in slides having a downslope buttress (Fig. 4c, Mourgues and Cobbold, 2006a; Mourgues et al., 2009). The presence of such a downslope buttress adds a resisting force similar to the effect of cohesion in the wedge. The sliding mass then comprises three distinct domains: an extensional domain upslope, a non-deformed slab at mid-slope, and a contractional domain downslope (Mourgues and Cobbold, 2006a; Mourgues et al., 2009; Lacoste et al., 2012).

3.2. Conditions for shallow sliding

In non-cohesive wedges, if pore pressure within the wedge becomes too large, the factor of safety *FS* reaches values of 1 (Eq. (12)) and the surface becomes unstable, thus triggering shallow slides. Detachments form parallel to the surface at any depth (Fig. 5a). The critical pore pressure ratio (λ_c^{*nc}) required to trigger such shallow sliding in non-cohesive material can easily be found (Hubbert and Rubey, 1959; Mandl and Crans, 1981) by considering failure on a plane parallel to the surface:

$$\sigma'_{xz} = \mu\sigma'_{zz} \quad (18)$$

Replacing σ'_{zz} and σ'_{xz} with expressions A1 and A2 (see Appendix A) leads to:

$$\lambda_c^{*nc} = 1 - \frac{\tan\alpha}{\tan\phi} \quad (19)$$

Given that cohesion (C_o) increases the stability of the surface slope, we add cohesion to the failure criterion (Eq. (18)) and the critical pore pressure ratio becomes:

$$\lambda_c^* = 1 - \frac{\tan\alpha}{\tan\phi} + \frac{Co}{\rho' gz\cos\alpha\tan\phi} = \lambda_c^{*nc} + \frac{Co}{\rho' gz\cos\alpha\tan\phi} \quad (20)$$

Equation (20) shows that λ^*_c increases with C_o. Where $\lambda^* < \lambda^{*nc}_c$, the cover remains stable regardless of the depth. Where $\lambda^* > \lambda^{*nc}_c$, a detachment may form at depth Z_c (Fig. 5b):

$$z_c = \frac{C_o}{\left(\lambda^* - \lambda_c^{*nc}\right)\rho g\cos\alpha\tan\phi} \quad (21)$$

This critical depth varies with cohesion and pore pressure λ^* (Fig. 5c). When the pore pressure increases, slides may form closer to the surface. If the wedge is thinner than Z_c, it remains internally stable (Fig. 6b). At the rear of the wedge, where the thickness becomes larger than Z_c, a new detachment may form parallel to the surface and may promote the rooting of normal faults (Fig. 6c).

3.3. Shape of the normal faults

In the non-cohesive critical taper theory, the angle ψ_o between the maximum principal stress and the surface is constant through the wedge, and therefore normal faults are predicted to be straight. Their dip depends on the magnitude of pore-fluid overpressure λ^*, as argued by Mourgues and Cobbold (2003). More generally,

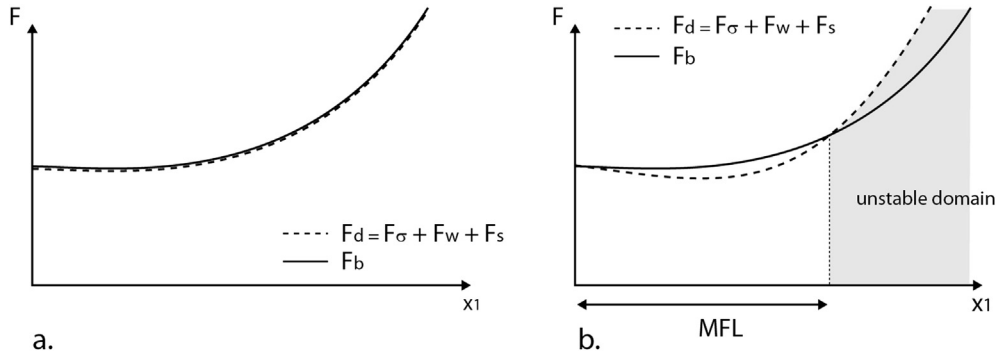

Fig. 3. Balance between driving forces $Fd = F\sigma + Fw + Fs$ and resisting forces Fb for a non-cohesive wedge satisfying equation (16) (**a**) and for a cohesive wedge requiring a Minimal Failure Length (MFL) (**b**).

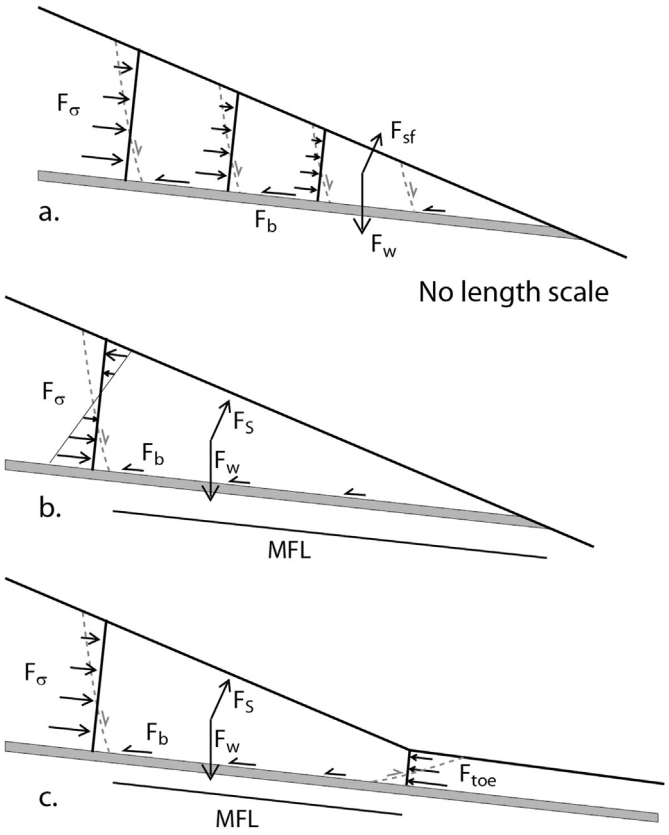

Fig. 4. Representation of the forces acting within a wedge (black), and respective patterns of deformation (grey) in the case of: (a) non-cohesive wedge, (b) cohesive wedge, (c) buttressed cohesive wedge.

Mourgues and Cobbold (2003) showed that the dips of normal faults in a sloping sedimentary sequence are controlled by the seepage forces induced by the pore-fluid overpressure gradient. They also showed that listric normal faults can form where permeability and pressure gradient (or λ^*) vary with depth.

In the case of a cohesive wedge, the non-linearity resulting from cohesion induces stress rotation and therefore listric faults, without any variation of λ^* with depth.

Fig. 7 shows the orientation of the faults relatively to the z-axis, as a function of depth z, determined using the following expressions from Mourgues and Cobbold (2003):

$$\tan(2\omega) = -2\sigma'_{xz}/(\sigma'_{xx} - \sigma'_{zz}) \quad (22)$$

and

$$\gamma = 45 - \phi/2 \quad (23)$$

where ω is the angle between σ_1 and the z-axis, and γ is the angle between σ_1 and the generated fault. In these expressions, the values of σ'_{zz}, σ'_{xz} and σ'_{xx} are calculated with equation (A1), A2 and A12, respectively (see Appendix A).

Two cases must be distinguished, depending on the value of λ^* and on the evolution of stresses with depth z (Figs. 6a and 7):

(1) Where $\lambda^* < \lambda^{*nc}_c$, stress rotation occurs mainly close to the surface, where the faults are steeper. At depth, where the influence of cohesion decreases, the orientation of the maximum principal stress tends towards ψ_o and the faults become straight (Figs. 6b and 7).
(2) Where $\lambda^* > \lambda^{*nc}_c$, the faults have a listric shape. This shape depends on the critical depth Z_c, where faults become parallel to the upper surface of the wedge (Figs. 6c and 7).

To test these last predictions, we used physical experiments involving pore-fluids in cohesive and permeable granular materials.

4. Analogue modelling

4.1. Experimental setup and procedure

Fluid overpressure has been successfully modelled through injection of compressed air in experimental studies (e.g., Cobbold and Castro, 1999; Cobbold et al., 2001, Mourgues and Cobbold, 2003, 2006a, 2006b; Mourgues et al., 2009; Lacoste et al., 2011, 2012)). Mourgues et al. (2014) were able to verify the predictions of the critical Coulomb wedge theory in the case of gravitational instabilities by performing scaled experiments with pore pressure under conditions close to the critical taper hypothesis. The main difficulty was that λ^* and λ^*_b must be constant within the wedge and along the detachment surface, respectively. In their experiments, the air pressure loss within the triangular edge of the model (Fig. 5b) had to be balanced by adding glass microbeads underneath (Mourgues et al., 2014).

However, even with such an apparatus, the basal pressure was not strictly constant and uncertainties on λ^*_b were strong (±0.1 for λ^*_b). For practical reasons, and because these uncertainties may arise with the use of cohesive material, we thought that it was not relevant to try to verify all the predictions of the cohesive model

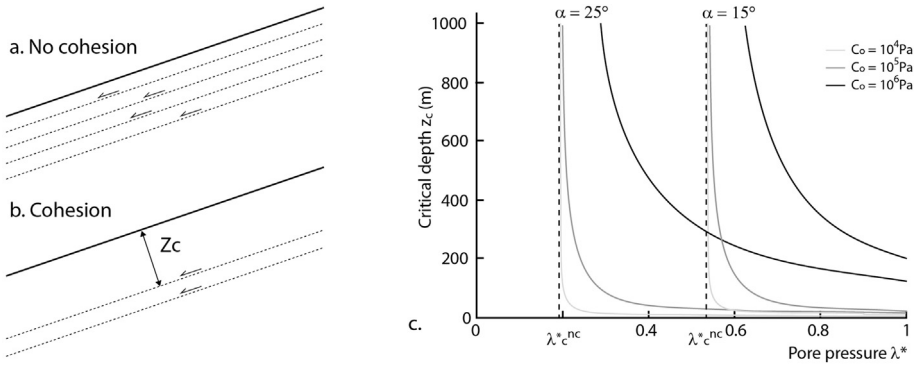

Fig. 5. a. In a non-cohesive system, the failure parallel to the upper surface can occur at any depth; b. In a cohesive system, the failure parallel to the upper surface will occur for depths equal or superior to a critical value (*Zc*); c. The critical depth *Zc* decreases exponentially with increasing λ^*, and is more easily attained in the case of steeper wedges ($>\alpha$) and smaller cohesions.

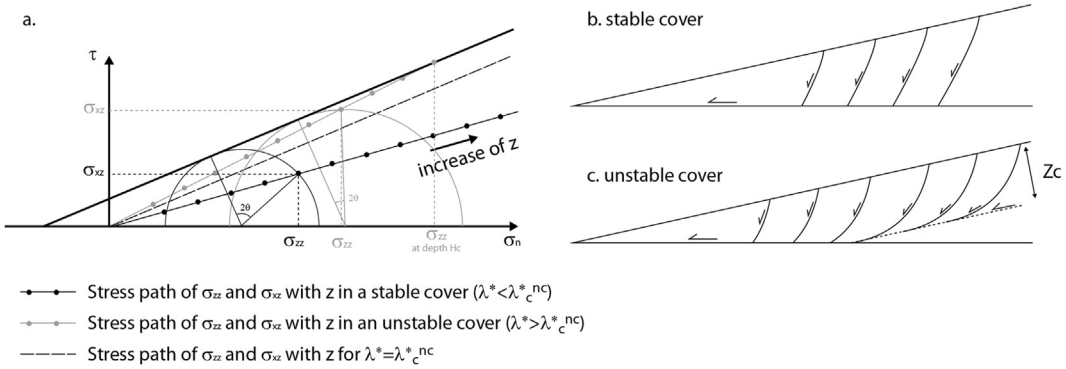

Fig. 6. a. Representation of the Mohr diagram for λ^* below, equal or above a critical λ^* value (λ^*_c). b. Where $\lambda^* < \lambda^*_c$, *Zc* is not attained within the wedge, and the faults do not become parallel to the upper surface of the wedge. c. Where $\lambda^* > \lambda^*_c$, *Zc* is attained within the wedge, and the faults become parallel to the upper surface of the wedge.

with such an experimental device. We therefore chose to verify only part of the predictions. Within the wedge itself, pore-fluid isobars are supposed to be parallel to the surface. This pore pressure condition can be easily applied on an analogue model. Thus, we focused on the stability of the surface and shape of normal faults.

In Mourgues and Cobbold (2003), extensional tests were performed in tilted tabular models of homogeneous non-cohesive materials (fine sand), with upward injection of compressed air to verify the structural consequences of pore-fluid pressures and seepage forces. Here, we report on similar tests performed using cohesive materials, to verify the formation of listric faults predicted by the analytical model (Section 3.3). The experimental setup was similar to that used in Mourgues and Cobbold (2003). We built a model made of cohesive material resting on two overlapping sieves. Beneath the sieves was a pressure chamber that provided a uniform fluid pressure at the base of the model. By slowly moving one of the sieves, we created a velocity discontinuity that induced the formation of normal faults (see Mourgues and Cobbold, 2003; for a complete description of the apparatus). The cohesive material was composed of fine glass microbeads. The cohesion ($C_o = 140 \pm 20$ Pa) and angle of internal friction ($\phi = 26°$) were determined with a series of direct shear tests on the material compacted to $\rho = 1600$ kg/m^3. The model was 5-cm thick. The microbeads layers were intercalated with dark thin layers of Silicon carbide, which served as markers of deformation. The model was then tilted 21°, so that Zc was close to the base of the model for reasonable values of λ^*, avoiding the risk of explosion due to high pore pressure (Mourgues and Cobbold, 2006a).

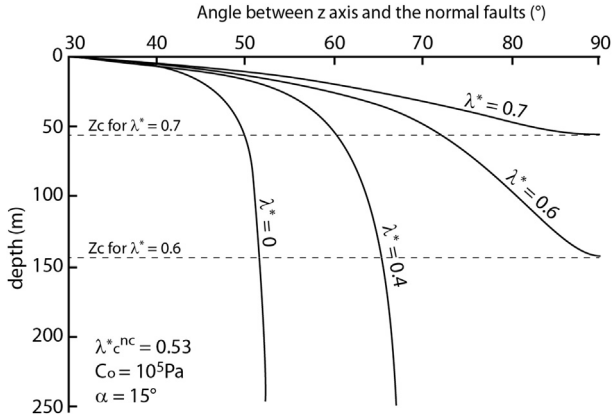

Fig. 7. Variation with depth of the angle between the z-axis and the faults for various λ^* values, with $\lambda^{*nc}_c = 0.53$. Notice the different shapes of the curves for λ^* higher and smaller than λ^{*nc}_c. For $\lambda^* < \lambda^{*n}_c$, faults are curve close to the surface and become straight at depth. For $\lambda^* > \lambda^{*n}_c$, faults flatten with depth becoming parallel to the surface at the corresponding value of Z_c.

Three different pore pressures were imposed at the base of the models: 0 Pa, 200 Pa and 400 Pa. These pressures correspond to λ^* values of 0, 0.25 ± 0.1 and 0.5 ± 0.1, respectively. Considering the uncertainties for the thickness and density of the model, and for the measurement of pore pressure, we estimated λ^* with an uncertainty of 0.1. Assuming $C_o = 140$ Pa, we estimated λ^{*nc}_c close to 0.21 and $\lambda^*_c = 0.6$ to activate a detachment along the base of the model.

4.2. Results and comparison with analytical predictions

In Fig. 8, we present the interpreted photographs taken during the experiments for the three different pore pressures. For $\lambda^* = 0$

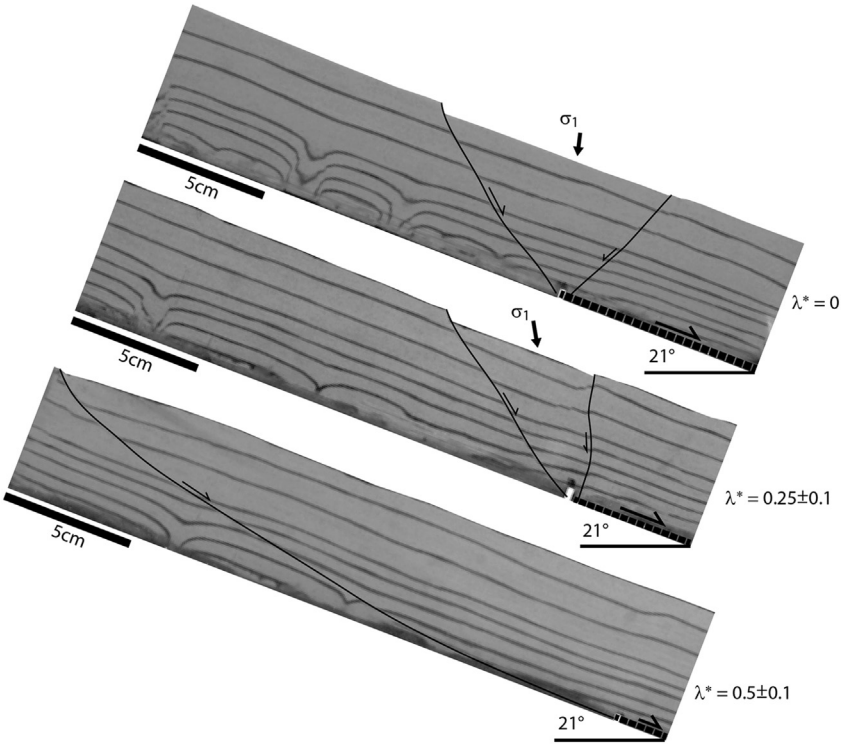

Fig. 8. Interpreted lateral photographs illustrating cross-sectional views of analogue models, with assumed material cohesion of 140 Pa, and λ^* values of 0, 0.25 ± 0.1 and 0.5 ± 0.1, respectively.

and $\lambda^* = 0.25$, conjugate faults formed at the velocity discontinuity. For $\lambda^* = 0.25$, one of the conjugate faults formed perpendicular to the slope. As a consequence, the dihedral angle between the conjugate faults is smaller than for $\lambda^* = 0$. Mourgues and Cobbold (2003) also made the same observation in their sand models, and explained this decrease of the dihedral angle as a consequence of an increase of the internal friction for very low effective stresses (due to pore pressure). If we assume that the principal effective stress σ_1 bisects the dihedral angle, we can also notice a small rotation of the stresses (Fig. 8) in response to the seepage forces (Mourgues and Cobbold, 2003). For $\lambda^* = 0$ and $\lambda^* = 0.25$, the faults do not seem to be listric, which is not the case for the experiment involving the highest pore pressure $\lambda^* = 0.5$. In this experiment, the normal fault is clearly listric, very low angle and long.

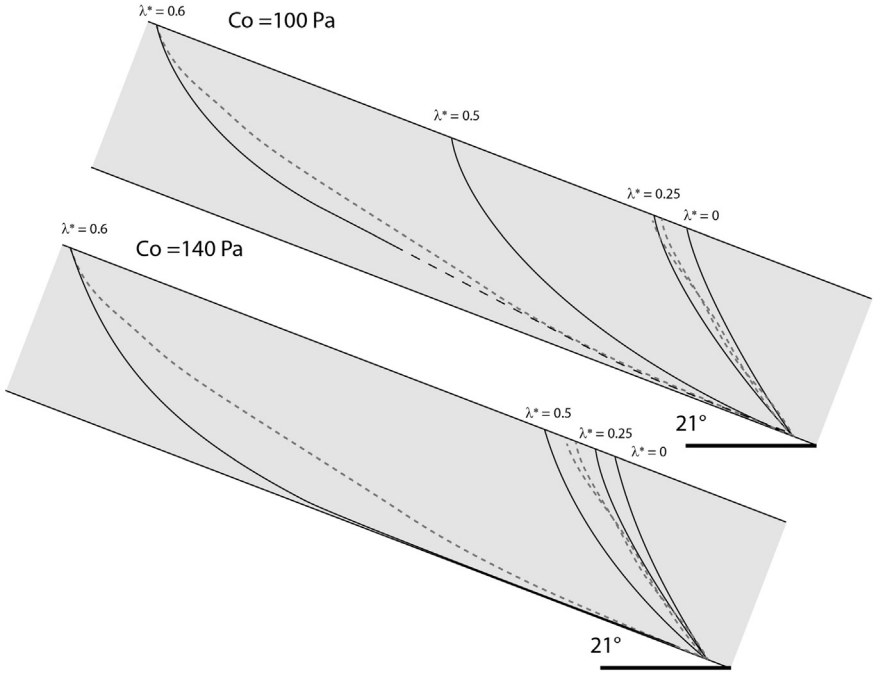

Fig. 9. Fault traces observed in the analogue experiments (dashed lines). Fault traces predicted by the analytical model for a hypothetical cohesion of 100 Pa (upper panel), and for the cohesion of 140 Pa assumed in the analogue tests (bottom panel).

Based on the analytical model, we determined the fault profiles expected for the different experimental tests (Fig. 9). Two cohesions were tested: 100 and 140 Pa. The predictions for $C_o = 100$ Pa seem to be in better agreement with the experimental data than for $C_o = 140$ Pa. For $\lambda^* = 0$ and $\lambda^* = 0.25$, the analytical model predicts the formation of normal faults with a very small curvature. The dips obtained for $C_o = 100$ Pa are in good agreement with the experimental faults. Where $C_o = 140$ Pa, the faults seem too steep. For $\lambda^* = 0.5$, comparison with the analytical model failed regardless of the cohesion value. By slightly increasing the pore pressure, λ^* exceeds the critical pressure λ^*_c to form a detachment at the base or within the model, so that the fault can migrate far from the velocity discontinuity. With $C_o = 140$ Pa and $\lambda^* = 0.6$, the detachment occurred at the base of the model. Nevertheless, the predicted fault is still too steep. For $C_o = 100$ Pa and $\lambda^* = 0.6$, $Zc = 3.6$ cm, so that a detachment parallel to the surface may form. The predicted shape of the normal fault for these conditions is in relatively good agreement with the experimental fault. The very low dip of the experimental fault is probably a good indication of the instability of the surface during extension. Nevertheless, a detachment parallel to the surface was not strictly observed, probably because the fault must root at the velocity discontinuity. This velocity discontinuity may also introduce stress perturbations in the model that could explain some of the discrepancies between the analogue results and the mathematically modelled faults.

5. Conclusions

We used an alternative derivation of the critical Coulomb wedge to analyse the structural effects of cohesion in an overpressured wedge subjected to gravitational deformation. The stabilizing effect of cohesion is accentuated in the foremost thin domain of the wedge, requiring a Minimum Failure Length (*MFL*) that controls the location of the first normal faults to form. This *MFL* decreases with smaller cohesion, smaller coefficient of internal friction, larger fluid overpressure ratio and steeper upper and basal surfaces of the wedge. Despite the mechanical properties of the wedge being assumed as homogeneous, non-linearity induced by cohesion results in the formation of listric faults. Their location within the wedge and fluid overpressure ratio control the fault shape. We observe two kinds of listricity: curvature close to the surface or curvature at depth, depending on cohesion, pore-fluid overpressure, and stability of the surface. Pronounced curvatures of the faults reflect a high degree of instability of surficial part of the wedge. This last prediction was verified with experiments involving pore pressure, but further analyses and comparison with natural examples are required to validate its use as a criterion in structural analysis to evaluate slope stability.

Acknowledgments

ACGC benefited from a PhD scholarship funded by FCT (SFRH/BD/68983/2010). FOM benefited from a sabbatical fellowship (SFRH/BSAB/1405/2014) awarded by FCT, Portugal. The experiments and the analytical developments were done at the Université du Maine (France). We thank Cédric Bulois and Christelle Gruber for the support in the experimental work.

Appendix A. Solution to the force balance including cohesive and non cohesive materials

We consider a wedge (Fig. 1a) with an upper surface angle α and basal surface angle β, both surfaces dipping in the same sense, and thus both angles are considered as positive. The Cartesian coordinate system x,z is defined with components parallel (x) and perpendicular (z) to the wedge's upper surface. The Cartesian coordinate system x_1,z_1 is defined with components parallel (x_1) and perpendicular (z_1) to the wedge's basal surface. The prism length (l) and height (h) are defined perpendicularly to the wedge's basal surface (Fig. 1b).

Following Mourgues et al. (2014), we establish the equations of static equilibrium for the system relative to the Cartesian coordinate system x,z, and we define as boundary conditions such that: (1) there is no variation of stresses along the x axis; (2) for $z = 0$ the effective stress components are null; and (3) the fluid overpressure ratio λ^* is constant within the wedge (the pore-fluid pressure is assumed to increase linearly with z).

In that case, stresses σ'_{zz} and σ'_{xz} are (Dahlen, 1984):

$$\sigma'_{zz} = \left(1 - \lambda^*\right)\rho' g z \cos(\alpha) \tag{A1}$$

$$\alpha'_{xz} = \rho' g z \sin(\alpha) \tag{A2}$$

Considering these effective stress components (Eqs. A1 and A2) and that the wedge is on the verge of failure everywhere (Dahlen, 1984), the analysis of the Mohr diagram allows the determination of σ'_{xx}. From geometrical considerations, the σ'_{xx} solutions can be found by expressing the radius (r) of the Mohr circle in two ways (Fig. A1).

$$1\text{- In triangle } O - B - \sigma'_o : r = \left(T + \sigma'_o\right)\sin\phi \tag{A3}$$

$$2\text{- In triangle } \sigma'_o - A - \sigma'_{zz} : r = \sqrt{\left(\sigma'_{xz}{}^2 + \left(\sigma'_{zz} - \sigma'_o{}^2\right)\right)} \tag{A4}$$

With σ'_o the center of the circle and T the tensile strength expressed in the linear Coulomb failure criterion as:

$$T = C_o \tan(\phi) \tag{A5}$$

By equalizing these two expressions, a second order equation is found:

$$A\sigma'_o 2 + B\sigma'_o + C = 0 \tag{A6}$$

with

$$A = \cos^2(\phi) \tag{A7}$$

$$B = -2\left(\sigma'_{zz} + T\sin^2(\phi)\right) \tag{A8}$$

$$C = \sigma'_{zz}{}^2 + \sigma'_{xz}{}^2 - T^2\sin^2(\phi) \tag{A9}$$

Discriminant of equation (A6) is

$$\Delta = B^2 - 4AC \tag{A10}$$

and solutions are:

$$\sigma_0 = \frac{-B \pm \sqrt{\delta}}{2A} \tag{A11}$$

σ'_{xx} is then deduced from:

$$\sigma'_{xx} = 2\sigma'_o - \sigma'_{zz} \tag{A12}$$

In the case where the wedge is not cohesive ($C_o = 0$), a simple expression of σ'_{xx} can be found (Mourgues et al., 2014):

$$\sigma'_{xx} = \sigma'_{zz}\left(2\frac{1 \pm \sin\phi\sqrt{1 - FS^2}}{\cos^2(\phi)} - 1\right) \tag{A13}$$

Afterwards, it is necessary to transform the stress components from (x,y) coordinate system to (x_1,z_1) coordinate system in order to proceed to the stability analysis of the wedge along the basal

detachment:

$$\sigma'_{x_1x_1}=\frac{\sigma'_{xx}+\sigma'_{zz}}{2}+\frac{\sigma'_{xx}-\sigma'_{zz}}{2}\cos(-2(\alpha-\beta))+\sigma'_{xz}\sin(-2(\alpha-\beta)) \quad (A14)$$

$$\sigma'_{z_1z_1}=\frac{\sigma'_{xx}+\sigma'_{zz}}{2}-\frac{\sigma'_{xx}-\sigma'_{zz}}{2}\cos(-2(\alpha-\beta))+\sigma'_{xz}\sin(-2(\alpha-\beta)) \quad (A15)$$

$$\sigma'_{x_1z_1}=\frac{\sigma'_{xx}+\sigma'_{zz}}{2}\sin(-2(\alpha-\beta))+\sigma'_{xz}\cos(-2(\alpha-\beta)) \quad (A16)$$

The assessment of the stability state of the wedge is made through the balance between the forces driving (F_d) and inhibiting (F_b) the downslope movement along the basal detachment (Fig. 1b).

F_d is the result of the sum of the driving force components along x_1 axis (Fig. 1b):

$$F_d = F_\sigma + F_w^{x1} + F_s^{x1} \quad (A17)$$

a) F_σ corresponds to the integral of $\sigma'_{x_1x_1}$ along the local wedge height (h, along the z_1 axis):

$$F_\sigma = \int_0^h \sigma'_{x_1x_1}\,dz_1 \quad (A18)$$

b) F_w^{x1} at a point along the basal detachment of length l and height h corresponds to the component along $\times 1$ of the gravitational load of the wedge section comprehended between that point and the wedge tip ($l=0$, and $h=0$). Considering a unitary width wedge slice:

$$F_w^{x1} = 0.5\rho' ghl\sin(\beta) \quad (A19)$$

c) F_s^{x1} is the component of the seepage force (SF) parallel to x_1, considering a wedge slice of unitary width:

$$F_s = 0.5\lambda^*\rho' gh^2\cos(\alpha)\cos(\alpha-\beta) \quad (A20)$$

in which λ^* is the fluid overpressure ratio within the wedge.

F_b corresponds to the integral of the basal friction on the basal detachment:

$$F_b = \int_0^l \mu_b\sigma'_n\,dx_1 \quad (A21)$$

in which μ_b and λ^*_b correspond to the internal friction coefficient and the fluid overpressure ratio along the basal detachment, respectively; σ'_n is the normal effective stress acting on the basal detachment of the wedge, taking into account a possible difference between λ^* and λ^*_b.

$$\sigma'_n = \sigma'_{z1z1} - (Pb - P) = \sigma'_{z1z1} + \left(\lambda^* - \lambda^*_b\right)\rho' gz\cos(\alpha) \quad (A22)$$

where P_b is the pore pressure within the detachment and P the pore-fluid pressure just above the detachment within the wedge.

In case where there is no cohesion, simple expressions of $\sigma'_{x_1x_1}$, $\sigma'_{z_1z_1}$ and $\sigma'_{x_1z_1}$ can be found from equations A1-2, A13 and A14-A16:

$$\sigma'_{x1x1} = E_3\rho' gz\cos(\alpha) \quad (A23)$$

$$\sigma'_{z1z1} = E_1\rho' gz\cos(\alpha) \quad (A24)$$

$$\sigma'_{x1z1} = E_2\rho' gz\cos(\alpha) \quad (A25)$$

F_σ and F_b are then analytically solved:

$$F_\sigma = 0.5E_3\rho' gh^2\cos(\alpha)\cos(\alpha-\beta) \quad (A26)$$

$$F_b = 0.5\mu_b\left(E_1 - \lambda^* + \lambda^*_b\right)\rho gl^2\cos(\alpha)\sin(\alpha-\beta) \quad (A27)$$

Finally, the exact solution of the force balance is easily found. Its expression is given in the main text (Eq. (17)).

For a cohesive wedge, there is no simple expression of σ'_{xx}, $\sigma'_{x_1x_1}$ or $\sigma'_{z_1z_1}$. Consequently, F_d and F_b must be numerically integrated and the final balance of forces (Eq. (13)) must be numerically solved.

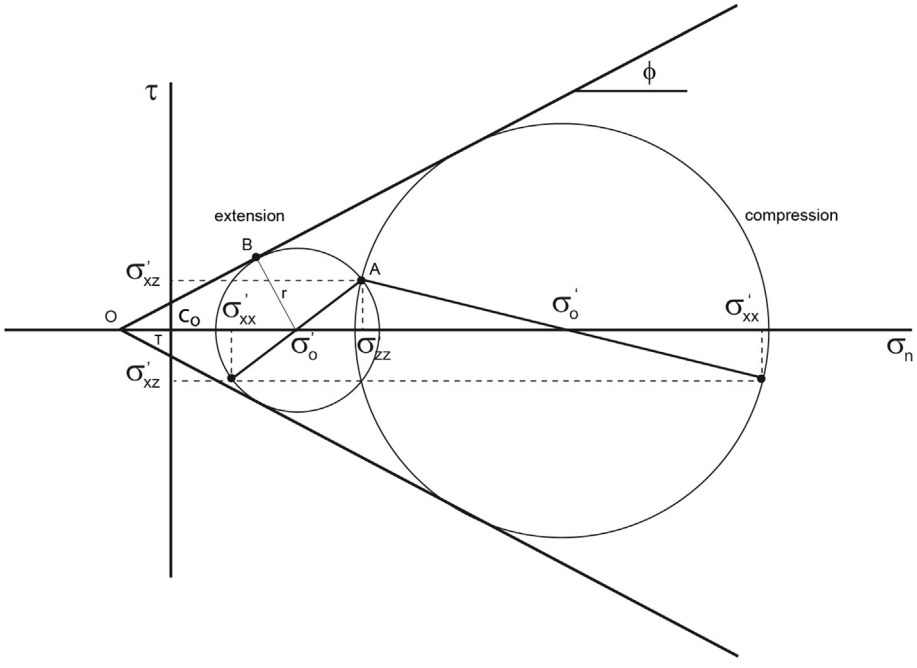

Fig. A1. Graphical determination of σ'_{xx} using Mohr circles.

References

Bryn, P., Berg, K., Forsberg, C.F., Solheim, A., Kvalstad, T.J., 2005. Explaining the Storegga slide. Mar. Pet. Geol. 22, 11–19. http://dx.doi.org/10.1016/j.marpetgeo.2004.12.003.

Cobbold, P.R., Castro, L., 1999. Fluid pressure and effective stresses in sandbox models. Tectonophysics 301, 1–19.

Cobbold, P.R., Durand, S., Mourgues, R., 2001. Sandbox modelling of thrust wedges with fluid-assisted detachments. Tectonophysics 334, 245–258.

Cobbold, P.R., Mourgues, R., Boyd, K., 2004. Mechanism of thin-skinned detachment in the Amazon fan: assessing the importance of fluid overpressure and hydrocarbon generation. Mar. Pet. Geol. 21, 1013–1025.

Cobbold, P.R., Zanella, A., Rodrigues, N., Loseth, H., 2013. Bedding-parallel fibrous veins (beef and cone-in-cone): worldwide occurrence and possible significance in terms of fluid overpressure, hydrocarbon generation and mineralization. Mar. Pet. Geol. 43, 1–20. http://dx.doi.org/10.1016/j.marpetgeo.2013.01.010.

Costa, A.C.G., Marques, F.O., Hildenbrand, A., Sibrant, A.L.R., Catita, C.M.S., 2014. Large-scale catastrophic flank collapses in a steep volcanic ridge: the Pico–Faial Ridge, Azores Triple Junction. J. Volcanol. Geotherm. Res. 272, 111–125. http://dx.doi.org/10.1016/j.jvolgeores.2014.01.002.

Dahlen, F.A., 1984. Noncohesive critical coulomb wedges: an exact solution. J. Geophys. Res. 89 (B12), 10125–10133.

Dahlen, F.A., 1990. Critical taper model of fold-and-thrust belts and accretionary wedges. Annu. Rev. Earth Planet. Sci. 18, 55–99.

Dahlen, F.A., Suppe, J., Davis, D., 1984. Mechanics of fold-and-Thrust belts and accretionary wedges: cohesive Coulomb theory. J. Geophys. Res. 89 (B12), 10087–10101.

Davis, D., Suppe, J., Dahlen, F.A., 1983. Mechanics of fold-and-thrust belts and accretionary wedges. J. Geophys. Res. 88 (B2), 1153–1172.

Day, S.J., 1996. Hydrothermal pore fluid pressure and the stability of porous, permeable volcanoes. In: McGuire, W.J., Jones, A.P., Neuberg, J. (Eds.), Volcano Instability on the Earth and Other Planets. Geological Society Special Publication, London, pp. 77–93.

del Potro, R., Hürlimann, M., Pinkerton, H., 2013. Modelling flank instabilities on stratovolcanoes: parameter sensitivity and stability analyses of Teide, Tenerife. J. Volcanol. Geotherm. Res. 256, 50–60. http://dx.doi.org/10.1016/j.jvolgeores.2013.02.003.

Elsworth, D., Voight, B., 1996. Evaluation of volcano flank instability triggered by dyke intrusion. In: McGuire, W.J., Jones, A.P., Neuberg, J. (Eds.), Volcano Instability on the Earth and Other Planets. Geological Society Special Publication, London, pp. 45–53.

Flemings, P.B., Long, H., Dugan, B., Germaine, J., John, C.M., Behrmann, J.H., Sawyer, D., IODP Expedition 308 Scientists, 2008. Pore pressure penetrometers document high overpressure near the seafloor where multiple submarine landslides have occurred on the continental slope, offshore Louisiana, Gulf of Mexico. Earth Planet. Sci. Lett. 269 (3–4), 309–325. http://dx.doi.org/10.1016/j.epsl.2007.12.005.

Haflidason, H., Sejrup, H.P., Nygard, A., Mienert, J., Bryn, P., Lien, R., Forsberg, C.F., Berg, K., Masson, D., 2004. The Storegga slide: architecture, geometry and slide development. Mar. Geol. 213, 201–234. http://dx.doi.org/10.1016/j.margeo.2004.10.007.

Hildenbrand, A., Marques, F.O., Catalão, J., Catita, C.M.S., Costa, A.C.G., 2012. Large-scale active slump of the southeastern flank of Pico Island, Azores. Geology 40 (10), 939–942. http://dx.doi.org/10.1130/G33303.1.

Hubbert, M.K., Rubey, W.W., 1959. Role of fluid pressure in mechanics of overthrust faulting. Geol. Soc. Am. Bull. 70, 115–166.

Iverson, R.M., 1995. Can magma-injection and groundwater forces cause massive landslides on Hawaiian volcanoes? J. Volcanol. Geotherm. Res. 66, 295–308.

Kvalstad, T.J., Andresena, L., Forsberga, C.F., Bergb, K., Brynb, P., Wangen, M., 2005a. The Storegga slide: evaluation of triggering sources and slide mechanics. Mar. Pet. Geol. 22, 245–256.

Kvalstad, T.J., Nadim, F., Kaynia, A.M., Mokkelbost, K.H., Bryn, P., 2005b. Soil conditions and slope stability in the Ormen Lange area. Mar. Pet. Geol. 22, 299–310. http://dx.doi.org/10.1016/j.marpetgeo.2004.10.021.

Lacoste, A., Loncke, L., Chanier, F., Bailleul, J., Vendeville, B.C., Mahieux, G., 2009. Morphology and structure of a landslide complex in an active margin setting: the Waitawhiti complex, North Island, New Zealand. Geomorphology 109, 184–196. http://dx.doi.org/10.1016/j.geomorph.2009.03.001.

Lacoste, A., Vendeville, B.C., Loncke, L., 2011. Influence of combined incision and fluid overpressure on slope stability: experimental modelling and natural applications. J. Struct. Geol. 33, 731–742.

Lacoste, A., Vendeville, B.C., Mourgues, R., Loncke, L., Lebacq, M., 2012. Gravitational instabilities triggered by fluid overpressure and downslope incision—Insights from analytical and analogue modelling. J. Struct. Geol. 42, 151–162.

Lehner, F.K., 1986. Comments on "noncohesive critical Coulomb wedges: an exact solution" by F.A. Dahlen. J. Geophys. Res. 91 (B1), 793–796.

Mandl, G., Crans, W., 1981. Gravitational gliding in deltas. In: McClay, K.R., Price, N.J. (Eds.), Thrust and Nappe Tectonics, Geological Society Special Publication, vol. 9, pp. 41–54.

Masson, D.G., Harbitz, C.B., Wynn, R.B., Pedersen, G., Lovholt, F., 2006. Submarine landslides: processes, triggers and hazard prediction. Philos. Trans. R. Soc. A 364, 2009–2039. http://dx.doi.org/10.1098/rsta.2006.1810.

Moore, J.G., Clague, D.A., 2002. Mapping the Nuuanu and Wailau landslides in Hawaii. In: Takahashi, E., Lipman, P.W., Garcia, M.O., Naka, J., Aramaki, S. (Eds.), Hawaiian Volcanoes: Deep Underwater Perspectives, Geophysical Monograph Series, 128. American Geophysical Union, Washington D.C., pp. 223–244. http://dx.doi.org/10.1029/GM128

Moore, J.G., Clague, D.A., Holcomb, R.T., Lipman, P.W., Normark, W.R., Torresan, M.E., 1989. Prodigious submarine landslides on the Hawaiian Ridge. J. Geophys. Res. Solid Earth 94 (B12), 17465–17484. http://dx.doi.org/10.1029/JB094iB12p17465.

Morgan, J.K., Moore, G.F., Clague, D.A., 2003. Slope failure and volcanic spreading along the submarine south flank of Kilauea volcano, Hawaii. J. Geophys. Res. 108 (B9), 2415. http://dx.doi.org/10.1029/2003JB002411.

Mourgues, R., Cobbold, P.R., 2003. Some tectonic consequences of fluid overpressures and seepage forces as demonstrated by sandbox modeling. Tectonophysics 376, 75–97.

Mourgues, R., Cobbold, P.R., 2006a. Sandbox experiments on gravitational spreading and gliding in the presence of fluid overpressures. J. Struct. Geol. 28, 887–901.

Mourgues, R., Cobbold, P.R., 2006b. Thrust wedges and fluid overpressures: sandbox models involving pore fluids. J. Geophys. Res. 111, B05404. http://dx.doi.org/10.1029/2004JB003441.

Mourgues, R., Lecomte, E., Vendeville, B., Raillard, S., 2009. An experimental investigation of gravity-driven shale tectonics in progradational delta. Tectonophysics 474, 643–656.

Mourgues, R., Lacoste, A., Garibaldi, C., 2014. The Coulomb critical taper theory applied to gravitational instabilities. J. Geophys. Res. Solid Earth 119 (1), 754–765. http://dx.doi.org/10.1002/2013JB010359.

Quidelleur, X., Hildenbrand, A., Samper, A., 2008. Causal link between Quaternary paleoclimatic changes and volcanic islands evolution. Geophys. Res. Lett. 35, L02303. http://dx.doi.org/10.1029/2007GL031849.

Reid, M.E., 2004. Massive collapse of volcano edifices triggered by hydrothermal pressurization. Geology 32 (5), 373–376. http://dx.doi.org/10.1130/G20300.1.

Satake, K., Smith, J.R., Shinozaki, K., 2002. Three-dimensional reconstruction and tsunami model of the Nuuanu and Wailau giant landslides, Hawaii. In: Takahashi, E., Lipman, P.W., Garcia, M.O., Naka, J., Aramaki, S. (Eds.), Hawaiian Volcanoes: Deep Underwater Perspectives, Geophysical Monograph Series 128. American Geophysical Union, Washington D.C., pp. 333–346. http://dx.doi.org/10.1029/GM128

Smith, D.E., Harrison, S., Jordan, J.T., 2013. Sea level rise and submarine mass failure on open continental margins. Quat. Sci. Rev. 82, 93–103. http://dx.doi.org/10.1016/j.quascirev.2013.10.012.

Voight, B., Elsworth, D., 1997. Failure of volcano slopes. Géotechnique 47 (1), 1–31.

Walder, J., Nur, A., 1984. Porosity reduction and crustal pore pressure development. J. Geophys. Res. 89 (B13), 11539–11548.

Wang, K., He, J., Hu, Y., 2006. A note on pore fluid pressure ratios in the Coulomb wedge theory. Geophys. Res. Lett. 33, L19310.

Yuan, X.P., Leroy, Y.M., Maillot, R., 2015. Tectonic and gravity extensional collapses in overpressured cohesive and frictional wedges. J. Geophys. Res. http://dx.doi.org/10.1002/2014JB011612.

Zanella, A., Cobbold, P.R., Rojas, L., 2014a. Beef veins and thrust detachments in Early Cretaceous source rocks, foothills of Magallanes-Austral Basin, southern Chile and Argentina: structural evidence for fluid overpressure during hydrocarbon maturation. Mar. Pet. Geol. 55, 250–261. http://dx.doi.org/10.1016/j.marpetgeo.2013.10.006.

Zanella, A., Cobbold, P.R., Le Carlier de Veslud, C., 2014b. Physical modelling of chemical compaction, overpressure development, hydraulic fracturing and thrust detachments in organic rich source rock. Mar. Pet. Geol. 55, 262–274. http://dx.doi.org/10.1016/j.marpetgeo.2013.12.017.